Meso-Superstructured Perovskite Solar Cells: Revealing the Role of the Mesoporous Layer

Daniel Ramirez,[a*] Kelly Schutt,[b] Juan Felipe Montoya,[a] Santiago Mesa,[a] JongChul Lim,[b] Henry J. Snaith,[b] and Franklin Jaramillo,[a*]

a. Centro de Investigación, Innovación y Desarrollo de Materiales – CIDEMAT, Facultad de Ingeniería, Universidad de Antioquia UdeA, Calle 70 No. 52-21, Medellín, Colombia.

b. Department of Physics, University of Oxford, Clarendon Laboratory, Oxford, United Kingdom.

D.R. Author 1, K.S. Author 2, J.F.M. Author 3, S.M. Author 4, J.L. Author5, H.J.S. Author 6, F.J. Author 7.
*Corresponding authors:
D.R.: estiben.ramirez@udea.edu.co
F.J.: franklin.jaramillo@udea.edu.co

Abstract

While perovskite solar cells (PSCs) have been developed with different device architectures, mesoporous devices have provided the highest power conversion efficiencies. In this work, thee working mechanism of both p-i-n and n-i-p meso-superstructured (MSSC) PSCs, which include a thin interlayer of porous alumina at the bottom electrode is explored. Interestingly, both positive-intrinsic-negative (p-i-n) and negative-intrinsic-positive (n-i-p) architecture, the mesoporous configuration was more efficient than its planar counterpart. For MSSC SnO_2-based n-i-p devices, that result was primarily due to an increase in V_{oc} and J_{sc}, resulting from improved band alignment and filling of the electron trap states (n-doping at the SnO_2/perovskite interface), which led to devices with 21.0 % efficiency and 20.3 % stabilized power output (SPO). Although MSSC NiO_x-based p-i-n meso-superstructured devices were less efficient due to lower V_{oc}, a slightly higher J_{sc} and fill factor improvement was achieved by the Al_2O_3 mesoporous layer resulting in devices with 16.9% efficiency. Importantly, the electronic nature of the perovskite is dependent upon its physical confinement within a mesoporous scaffold. Therefore, either p-i or n-i perovskite/semiconductor interfaces can be engineered by selectively modifying the semiconductor behavior with the introduction of an insulting mesoporous scaffold interlayer.

1. Introduction

Metal halide perovskites have excited the global photovoltaic research community by achieving rapid gains in power conversion efficiency, going from just 3% in their first application in 2009[1] to over 23% more recently.[2,3] These unique organic-inorganic materials utilize Earth-abundant, low-cost elements in the ABX_3 perovskite structure where A is a small organic cation (typically Cs^+, $CH_3NH_3^+$, $CH(NH_2)_2^+$), B is a divalent metal cation (typically Pb^{2+} or Sn^{2+}), and X is the halide anion (I^-, Cl^-, Br^-). The rapid efficiency gains in perovskite solar cells can be attributed in large part to the desirable optoelectronic properties of these materials. Among these properties, a tunable band-gap, large dielectric constant, long carrier diffusion lengths, low non-radiative recombination, and high optical absorption make metal halide perovskites exceptional semiconductors for photovoltaic applications.[4–7] High quality metal halide perovskite thin films can be achieved with a variety of processing methods including vacuum evaporation and solution processing. Perovskite solar cells also have potential for commercial viability due to their low cost.[8,9]

While metal halide perovskites offer desirable optoelectronic properties, advancements in device architecture have also played a crucial role in the rapid efficiency improvements in perovskite photovoltaics. Initially, Miyasaka and co-workers utilized metal halide perovskites as light absorbing nanoparticles.[1] In 2012, mesoporous Titania (TiO_2) and Alumina (Al_2O_3) scaffolds were developed to achieve power conversion efficiencies of 9.2% and 10.9%, respectively, employing a solid-state hole-conductor.[10,11] While mesoporous devices had reduced hysteresis and improved charge extraction, planar devices fabricated with vapour deposition in 2013 boosted power conversion efficiency to 15.4%,[12] raising questions as to whether the mesoporous architecture was

necessary. While planar devices have made impressive gains since then,[13–15] the debate on the superior device architecture remains unsettled, with recent state-of-the-art devices still utilizing a thin mesoporous TiO_2 inter-layers and a solid perovskite capping layers,[2] which is an architecture first observed to work well with mesoporous alumina scaffolds.[16]

While mesoporous layers have typically been utilized in combination with compact TiO_2,[17] the surface defect density of TiO_2 and limited stability of perovskites in contact with this semiconductor have created concerns about the viability of this selective contact.[15,18] As alternative materials, other metal oxides have been used, including tin oxide (SnO_2),[19] which provides a higher performance alternative to TiO_2 with reduced hysteresis in planar heterojunction cells, and a simple chemical bath processing route offers a more scalable and higher performance route than atomic layer deposition.[20]

In this work, we develop n-i-p and p-i-n devices on planar and mesoporous Al_2O_3 scaffold architectures, referred as meso-superstructured (MSSC) architectures,[21] in order to gain a deeper understanding of the electronic role of the mesoporous insulating inter-layer. Utilizing kelvin probe force microscopy, we have discovered that the mesoporous layer can enhance the *p* or *n* nature of the perovskite, depending on the underlying semiconductor layer which it is crystallized. Upon NiO_x, the mesoporous layer induces *p* doping at the perovskite and therefore the external quantum efficiency (EQE) declines sharply at shorter wavelengths as the thickness of the scaffold layer is increased, corresponding this to photons that are absorbed near the interface. Regarding n-i-p architecture, where infiltrated perovskite crystallizes on n-type semiconductor, in our case SnO_2, the mesoporous layer strengthens the n-type behavior of perovskite at the semiconductor/mesoporous layer interface, improving the EQE for thin mesoporous layers; this result is consistent with findings that electron traps dominate and limit performance in metal halide

perovskites. Finally, for the first time, we apply this knowledge of the mesoporous doping effect by MSSC p-i-n and n-i-p devices with NiO_x and SnO_2, respectively, with optimized scaffold layer thicknesses. These interface modifications allowed us to improve the power conversion efficiency over the p-i-n and n-i-p planar devices, in the latter case from 20.2% to 21.0%, while boosting the stabilized power output from 19.0% to 20.3% for MSSCs.

2. Experimental Section

All chemicals were purchased from Sigma Aldrich unless stated otherwise.

2.1. Fabrication of n-i-p Devices

n-i-p devices were fabricated on top of Fluorine-doped tin oxide (FTO) coated glass substrates (Pilkington TEC 7). Substrates were scrubbed with detergent (2% Hellmanex in water) and then sequentially sonicated for 2 min in acetone, isopropyl alcohol, and nanopure deionized water. The FTO was treated in oxygen plasma for 10 min immediately prior to the spin-coating the SnO_2 electron transporting. For that, 0.05 M tin (IV) chloride pentahydrate ($SnCl_4 \cdot 5H_2O$) was dissolved in 2-propanol and stirred for 30 minutes. The solution was spin-coated onto FTO at 3000 rpm for 30 s. Substrates were dried at 100 °C for 10 min and then annealed at 180 °C for 60 min. Substrates were then treated with a chemical bath deposition. 1.25 g urea was dissolved in 100 ml nanopure deionized water. 25 μL of 3-mercaptoproprionic acid (99%, Alfa Aesar) and 1.25 mL HCl (37%, Alfa Aesar), 0.012 M $SnCl_2.2H_2O$ were added, and the solution was stirred vigorously for 2 min. The substrates were covered in the solution and placed in an oven at 70 °C for 3 h. Finally, the substrates were sonicated in deionized water for 2 min and then annealed again at 180 °C for 60 min. The substrates were treated with UV-ozone for 15 min immediately prior to perovskite or

Alumina deposition. The mesoporous Al_2O_3 layers were deposited by spin-coating solutions of commercial alumina nanoparticles dispersion (50 nm *Sigma Aldrich*) diluted at 1:20, 1:5 and 1:3 volume ratio of dispersion:isopropanol to give 50 nm, 100 nm and 200 nm. 1.45 M $FA_{0.83}Cs_{0.17}Pb(I_{0.83}Br_{0.17})_3$ precursor solution was prepared with 64 mg CsI (Alfa Aesar), 207 mg FAI (Dyesol), 538 mg PbI_2 (TCI), and 104 mg $PbBr_2$ (TCI). The perovskite solution was prepared in a mixture of anhydrous DMF (800 µL) and DMSO (200 µL). The precursor solution was stirred on a hot plate at 70 °C for 15 minutes. Room temperature precursor solution was deposited in a dry box (10-15% relative humidity) and spin-coated at 1000 rpm for 10 s and then at 6000 rpm for 35 s (ramp of 2000 rpm s^{-1}). 80 µL of anisole was quickly dispensed onto the substrate 10 s before the end of spin-coating, and then the substrate was annealed on a hot plate at 100 °C for 45 min. The hole transport material (HTM) 2,2',7,7'-tetrakis(N,N'-di-p-methoxyphenylamine)-9,9'-spirobifluorene (spiro-OMeTAD) was prepared by dissolving 85 mg spiro-OMeTAD (Lumtec) in 1 ml anhydrous chlorobenzene along with 20 µl lithium bis(trifluoromethanesulfonyl)imide (Li-TFSI) salt in acetonitrile (500 mg ml^{-1}) and 33 µL tert-butylpyridine (tBP). 100 µl of spiro-OMeTAD solution was statically dispensed onto the substrate and then spin-coated at 2000 rpm for 45 s. Finally, to complete the devices, 80 nm thick gold electrodes were thermally evaporated.

2.2. Fabrication of p-i-n Devices

P-i-n devices were fabricated on ITO coated glass (Naranjo). The substrates were washed with neutral soap (Inmunodet neutro) and sequentially sonicated in DI water, acetone and isopropanol for 5 minutes. Then, ultraviolet ozone (UVO) treatment was done for 5 min at 100 °C. The NiO_x hole transporting material was synthesized by using a chemical precipitation method previously

reported.[22,23] The resulting NiO_x powder was dispersed in deionized (DI) water to a 23 mg/mL concentration and spin coated at 3000 rpm for 30 s with a 3 s ramp. The mesoporous Al_2O_3 layers were deposited by spin-coating solutions of commercial alumina nanoparticles dispersion (50 nm *Sigma Aldrich*) diluted at 1:20, 1:5, 1:3 and 1:2 volume ratio of dispersion:isopropanol to give 50 nm, 100 nm, 200 nm and 400 nm films. These films were then dried overnight under ambient conditions. To obtain the perovskite layer, a precursor solution of methylammonium iodide (Dyesol) and lead iodide (Alfa Aesar; 1:1 molar ratio; 55 wt%) in N,N-dimethylformamide (DMF) was deposited by spin-coating at 4000 rpm for 25 s. During spinning, 500 µL of diethylether were dripped on the substrate after 10 seconds and the films were annealed at 65 °C for 1 min and 100 °C for 10 min. PCBM (1-Material) was deposited *via* spin-coating a 20 mg/mL solution in chlorobenzene (CB) at 2000 rpm for 30 s. Rhodamine 101 was deposited on top of the PCBM layer by spin coating a 0.5 mg/mL solution at 4000 rpm for 30 s. Finally, to complete the devices, a 100 nm thick silver electrodes were thermally evaporated under vacuum ($\approx 10^{-6}$ mbar) at a deposition rate around ≈ 0.1 nm/s.

2.3. Characterization

All the comparative characterization was performed to the same perovskite composition. AFM images were obtained in a MFP-3D infinity from Oxford Instruments. Optical absorption was measured in the range of 400-800 nm using a Cary 100 Agilent spectrometer, for the case of total reflectance an integrating sphere was employed. Surface roughness and thickness of the different layers were obtained using a Bruker DektakXT profilometer. Steady-state and time-resolved PL measurements were performed using a time resolved single-photon counting setup (FluoTime 300, PicoQuant GmbH) using a 507-nm laser head (LDH-P-C-510, PicoQuant GmbH) at frequencies

between 0.5 MHz and 2MHz with a pulse duration of 117 ps and fluence of 0.3 μJ/cm^2/pulse with a detection wavelength of 775 nm. For transient photoconductivity the Nd:YAG laser excitation source was tuned to 470 nm and pumped at 10 Hz with 7 ns pulses is used at the range of fluences to have various carrier density as described in the main text. This pulse light is illuminated in entire sample area to evenly excite the film. A bias of 24 V is applied across the in-plane (lateral) electrodes. Here, as the contact resistance between perovskite film and Au electrode is fairly small compared to sample resistance, we employ two electrode conductivity measurement. A variable resistor is in series with sample in the circuit to always be <1% of the sample resistance. We monitored the voltage drop across the variable series resistor through a parallel oscilloscope (1MΩ) to determine the potential dropped across the two in-plane Au electrodes (4mm channel length) in the sample. The perovskite film was scribed to have 4mm channel width, and coated with inert 200 nm PMMA. Transient photoconductivity ($s_{\text{Transient-Photo}}$) was calculated by the equation, $\sigma_{Ph} = \frac{\Delta V_{Osc}}{R_r \times (V_{bias} - V_{Osc})} \times \frac{l}{w \times t}$ where, R_r is variable resistor, V_{bias} is bias voltage, l is channel-channel length, w is channel width, and t is film thickness.

2.4. Solar cell characterization

Solar cells were measured with an Abet Class AAB solar simulator under simulated AM 1.5 sunlight at 100 mW cm^{-2} irradiance, calibrated by an NREL-calibrated KG5 filtered silicon reference cell. The mismatch factor was calculated at < 1%. J-V curves were recorded with a 2400 Series Sourcemeter by Keithly Instruments. The solar cell active area was 0.09 cm^2.

3. Results and discussion

Schematics of the p-i-n and n-i-p mesoporous device architectures are shown in **Figure 1**, along with their related performance data. The p-i-n devices were fabricated on nickel oxide (NiO_x),

utilizing $PC_{60}BM$ and Rhodamine as electron transport layers, while the n-i-p devices were fabricated on tin oxide (SnO_2), with Spiro-OMeTAD as a hole transport layer. The mesoporous layers were optimized by modifying the spin-coated solution concentration, and further details can be found in the ESI.

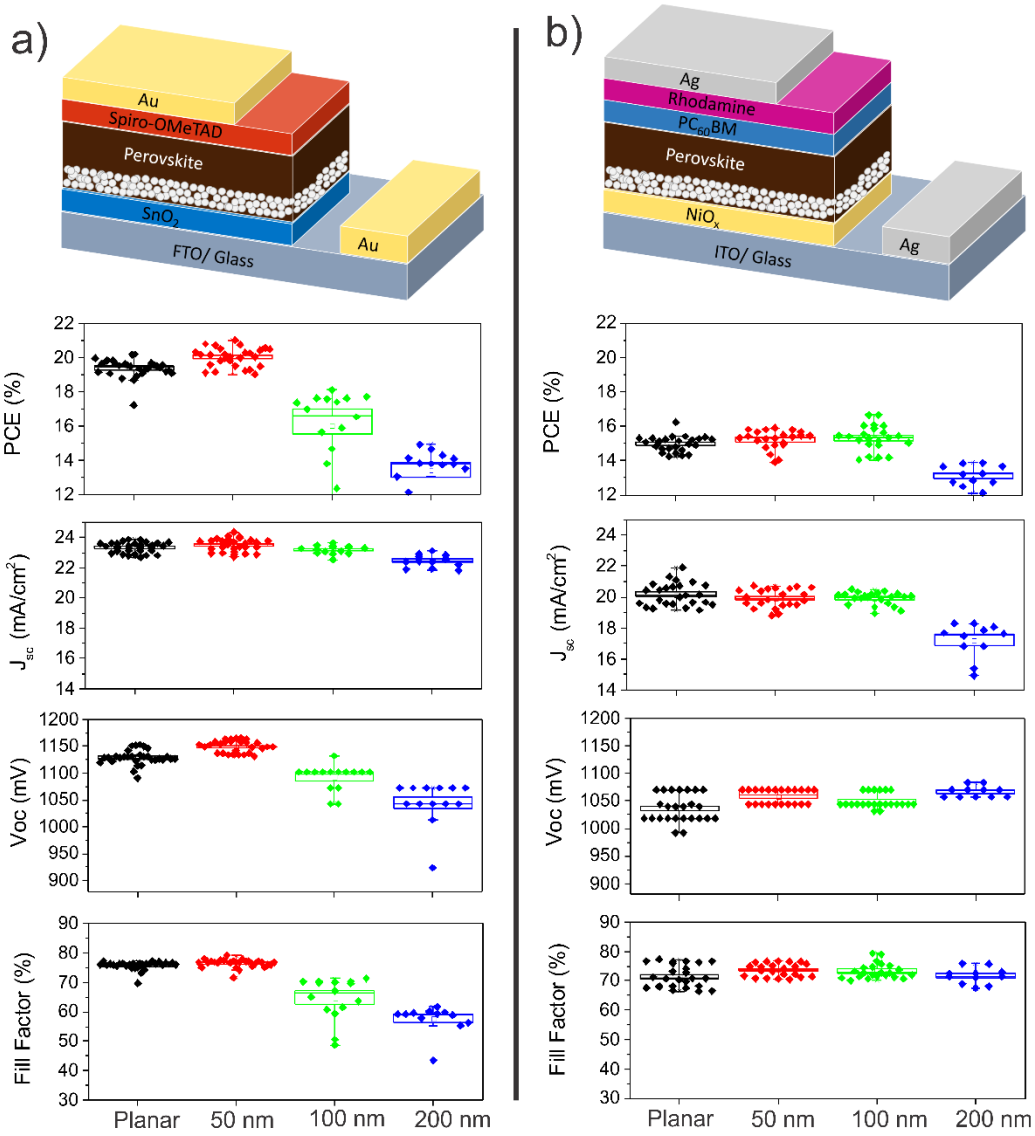

Figure 1. Comparative photovoltaic parameters for a) n-i-p and b) p-i-n devices with different mesoporous layer thicknesses.

Notably, at low mesoporous layer thicknesses V_{oc} and fill factor increased in both n-i-p and p-i-n devices, leading to maximum PCE of 21.0% and 16.9%, respectively (see **Table 1** for photovoltaic

parameters). However, as the mesoporous layer thickness increases, both the p-i-n and n-i-p devices exhibit reduced power conversion efficiency. As we will discuss in detail, this reduced efficiency can be attributed to lower current due to insufficient minority carrier diffusion length in the p-i-n devices, and increasing series resistance in the normal devices. These results also corroborate findings from Leijtens *et al.*[24] that sub-gap, trap mediated recombination is the dominant recombination mechanism in perovskite solar cells, with electron trapping being the primary decay pathway. Thus, one route to improving V_{oc} is reducing and filling electron traps, promoting bimolecular recombination.

Table 1. Solar cell performance parameters determined from *J–V* curves

Device	PCE (%)	Jsc (mA/cm2)	Voc (mV)	FF (%)
n-i-p planar				
Average	19.4±0.6	23.3±0.3	1128±14	75±2
Best	20.2	23.6	1126	76
n-i-p meso 50nm				
Average	20.1±0.6	23.5±0.4	1150±11	76±2
Best	21.0	24.3	1140	76
n-i-p meso 100nm				
Average	16.3±2.1	23.2±0.3	1095±24	69±7
Best	18.2	23.45	1135	71
n-i-p meso 200nm				
Average	16.3±2.1	23.2±0.3	1095±24	69±7
Best	18.2	23.45	1135	71
p-i-n planar				
Average	15.0±0.5	20.2±0.7	1026 ±25	71±4
Best	16.2	21.9	1018	73
p-i-n meso 50nm				
Average	15.23±0.6	19.9±0.6	1058±13	74±2
Best	16.2	20.7	1044	74
p-i-n meso 100nm				
Average	15.3±0.7	19.9±0.5	1061±12	74±2
Best	16.9	20.4	1080	76
p-i-n meso 200nm				
Average	12.5±1.3	16.9±1.3	1066±9	72±4
Best	13.9	18.3	1070	71
p-i-n meso 400nm				
Average	7.5±1.2	10.1±0.5	1040±9	72±9
Best	9.2	10.9	1044	80

In order to better understand the origin of performance differences in n-i-p and p-i-n mesoporous devices, we spin-coated diluted perovskite precursor onto Al_2O_3 mesoporous substrates to characterize the effects of the mesoporous layer on the perovskite (detailed experimental information in ESI, as well as raw KPFM images in **Figure S1** to **Figure S4**). As shown in **Figure 2a**, the perovskite infiltrating a mesoporous scaffold on NiO_x (p-type/Al_2O_3/perov) has a deeper work function of 5.21 eV than perovskite on planar NiO_x (p-type/perov) (5.16 eV), demonstrating greater *p-type* behaviour in the infiltrated one. Conversely, perovskite infiltrating a mesoporous scaffold of Al_2O_3 on the n-type semiconductor has a shallower work function of 4.63 eV, an n doping effect. Both, the p-i-n and n-i-p devices on mesoporous insulating scaffolds show improved V_{oc}, which we attribute to improved quasi-Fermi level splitting in the perovskite as a result of the modified work function.

In addition to measuring the work function shift with kelvin probe force microscopy, the perovskite-mesoporous interface was characterized with surface photovoltage (SPV) measurements at different illumination intensities, as shown in **Figure 2b**. As described elsewhere,[25] the SPV sign is related to the type of surface states while its magnitude relates to the density of states. A negative SPV corresponds to superficial acceptor states, capturing electrons at the surface (upward band bending) while a positive SPV signal corresponds to donor states, injecting electrons into the vicinity of the surface (downward bending).[26] Therefore, this technique allows confirmation of the p- or n-type surface characteristics of a semiconductor. Remarkably, for the reference perovskite grown on n-type and n-type/m-Al_2O_3 surfaces, the SPV showed a positive trend, commonly attributed to a p-type semiconductor surface,[27] with a magnitude of SPV

reaching a maximum of 117 ± 11 mV and 213 ± 13.9 mV, respectively. Additionally, the n-type/m-Al_2O_3 reached saturation in SPV with just 25% of illumination intensity, which means that there is a lower potential barrier for photogenerated carriers than for a planar n-type based device and that surface acceptor states are rapidly filled in concordance with the previously demonstrated perovskite grown on top of n-type/m-Al_2O_3.[28] These results are in total agreement with the n-i-p device operation for the common SnO_2/perovskite/Spiro-OMeTAD or SnO_2/m-Al_2O_3/perovskite/Spiro-OMeTAD configuration in which the perovskite should couple in the first side to the n-type SnO_2 and in the other side to the p-type Spiro-OMeTAD. For the case of the perovskite grown on p-type and p-type/m-Al_2O_3, SPV showed an opposite behaviour with a negative SPV. Even though the magnitude of the SPV was not very different between planar p-type and p-type/m-Al_2O_3, the alumina-based sample showed a faster saturation point at 50% illumination, while the bare NiO_x only started to show a saturation point at 100%. This indicates that Al_2O_3 can also fill trap states in the p-i-n configuration and that the device operation for a NiO_x/perovskite/PCBM or NiO_x/m-Al_2O_3/perovskite/PCBM corresponds to a more p-type perovskite contacting the NiO_x layer and an n-type perovskite contacting the PCBM layer. This result confirms that the semiconductor character of the infiltrated perovskite is mainly determined by the contacting semiconductor interface and not by the m-Al_2O_3 itself and that in both cases, p-i-n or n-i-p configurations can be obtained by using Al_2O_3 as scaffold material while improving the band alignment and reducing surface trap states.

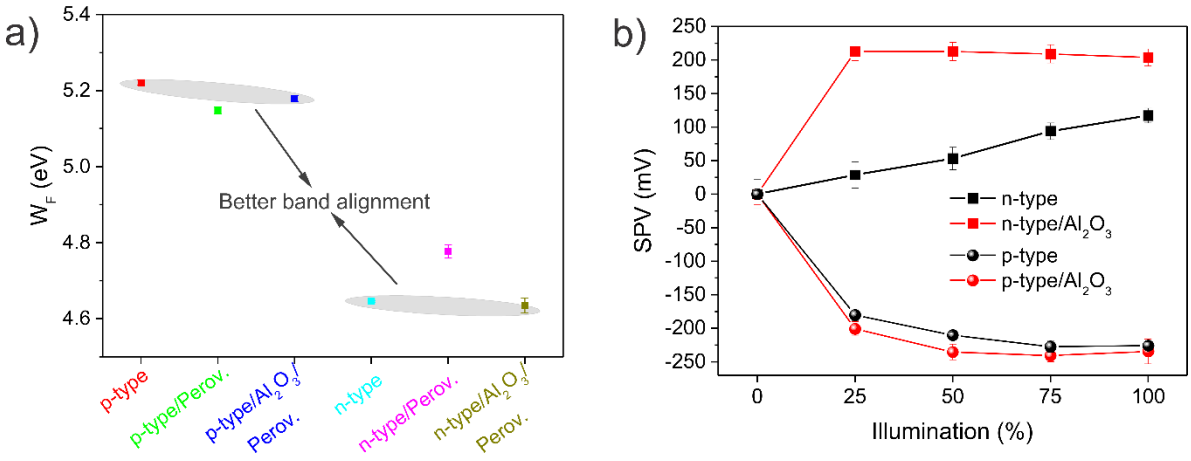

Figure 2. Surface electronic properties of the infiltrated perovskite**.** a) Work function of a thin layer of perovskite grown of top of p-type or n-type semiconductor evidencing the band alignment induced by the semiconductor and improved by the mesoporous layer, and b) surface photovoltage (SPV) analysis of a thick perovskite also indicates lower surface trap states induced by the alumina. Note: 100% illumination corresponds to 3mW/cm^2.

In **Figure 3** we examine the current voltage characteristics, EQE, and stabilized power output of planar and mesoporous solar cells. As discussed earlier, thin mesoporous layers improve V_{oc} in both the n-i-p and p-i-n devices. In the n-i-p devices, the thin mesoporous layer also improves current density, indicating improved charge extraction, but also a contribution from increased film thickness and light absorption (see **Figure S5** for a comparative cross section SEM image of the planar and mesoporous devices and top view SEM of the 50 nm and 100 nm Al_2O_3 mesoporous layer). In p-i-n mesoporous devices, current density decreases as the thickness of the mesoporous alumina layer is increased. In order to understand this effect more clearly, we fabricated p-i-n devices with 400 nm mesoporous Al_2O_3 (see **Figure S6** for full photovoltaic parameters). These devices had an average J_{sc} of 10.1 mA/cm^2, while keeping almost the same V_{oc} and FF as the planar heterojunction and thinner Al_2O_3 cells. We also noted that all the mesoporous thicknesses exhibit

the same overall specular reflectance (**Figure S7**), such that the large differences in photocurrent are not expected to come from differences in light absorption. However, since the introduction of the mesoporous layer increased the total thickness of the active layer and decreased the capping layer (Table S1), these results indicate that charge collection from within the mesoporous scaffold region, in the p-i-n architecture, is limited.

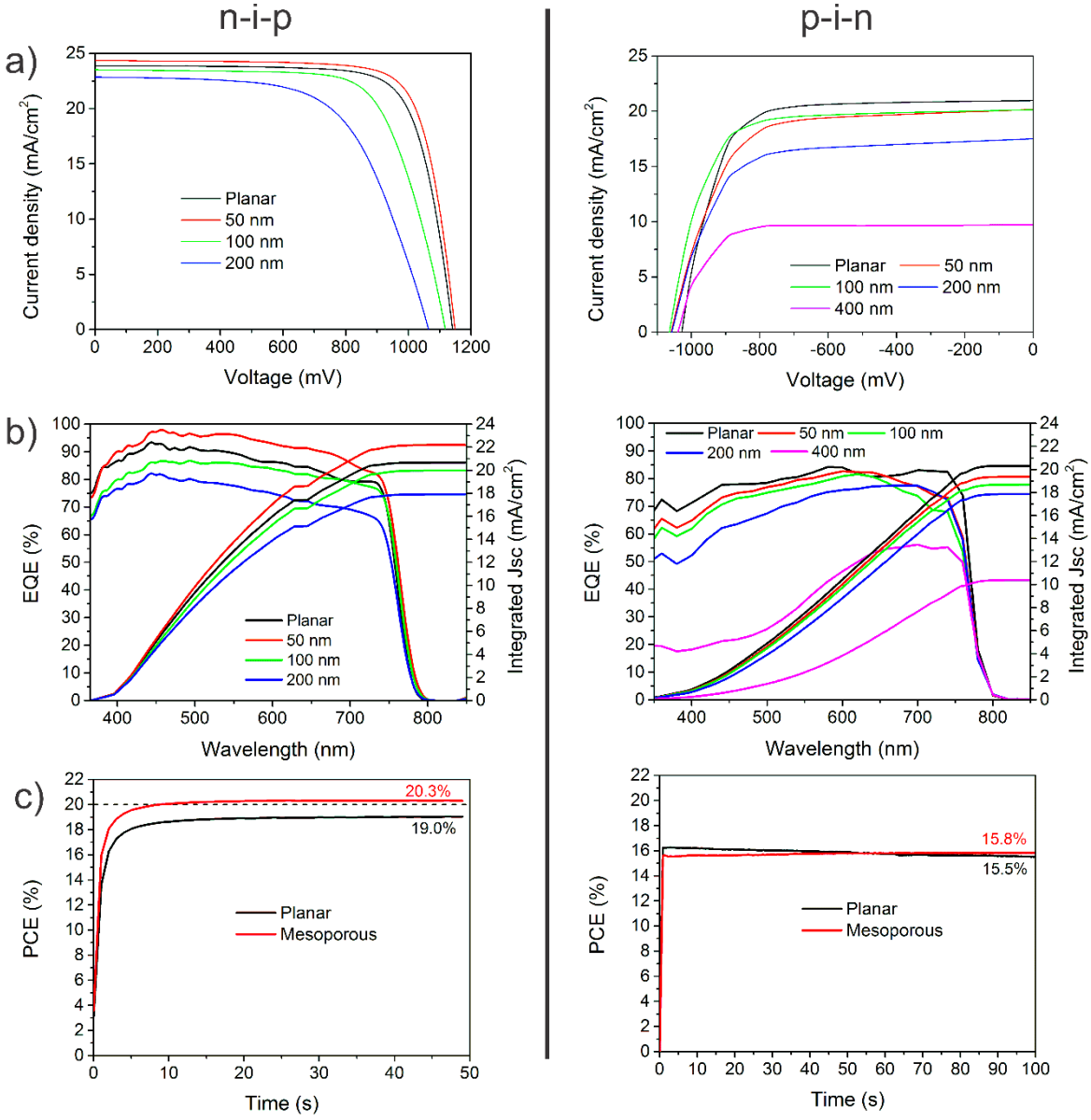

Figure 3. Comparative a) JV curves, b) EQE and c) SPO of n-i-p and p-i-n devices. Note that 400 nm Al_2O_3 p-i-n JV curve and EQE was added to show more clearly the reduction in photocurrent in the blue region.

The EQE graphs help to explain this difference in current between the two architectures by providing insight into the "minority carrier diffusion length". In the p-type perovskite film, absorption of shorter wavelengths near and within the mesoporous interface results in current losses with increasing mesoporous thickness. This is consistent with electron traps being the dominant non-radiative recombination pathway,[29] inhibiting the diffusion length of the minority carrier, which in this case are electrons. In the n-type perovskite film, absorption of shorter wavelengths near and within the mesoporous interface results in increased EQE. This indicates that both electrons and holes (the minority carrier in this case) have long diffusion lengths within the n-type perovskite region. The panchromatic improvement in photocurrent generation for the n-i-p cells, suggest that the charge collection efficiency is improved with the insertion of the mesoporous scaffold interlayer. This is consistent with the more n-type region of perovskite absorber, making improved, lower resistance electronic contact with the SnO_2 charge extraction layer. It is evident that n-i-p devices are more efficient than p-i-n devices, due to the lower V_{oc} obtained in NiO_x-based devices. The stabilized power output (SPO) of the best performing n-i-p meso-superstructured device with 50nm Al_2O_3 interlayer, was 20.3% compared to 19.0% of the planar counterpart. On the other hand the SPO for the p-i-n meso-superstructured devices 15.8% compared to 15.5% of the planar counterpart. Note the fast SPO stabilization of less than 2 seconds for the p-i-n devices; this is related to the absence of hysteresis in this device configuration and the common pronounced hysteresis of the n-i-p devices[18] as shown in **Figure S8,** which includes

representative curves both forward and reverse scans for the fabricated devices. In the latter case is reduced by the mesoporous layer.

The improved V_{oc} should be reflected in reduced non-radiative recombination. In order to corroborate this we performed steady and time resolved PL. As shown in **Figure 4a**, the perovskite deposited on top of glass showed an initial fast electron trapping process (around 40 ns lifetime). After this, the trapped electrons slowly recombine with free holes on tens of µs timescales, deviating significantly from the expected trap mediated recombination pathway, as also observed by *Leijtens et al*.[28] The perovskite deposited on top of a mesoporous Al_2O_3 layer, showed a slightly longer lifetime up to 1.5 µs, indicating that in this case more surface traps are probably filled,[30] resulting in a situation where most of the traps are filled at solar fluence, allowing the solar cells to obtain improved photovoltages, as previously observed. This is also in agreement with the higher steady state PL shown in **Figure S9**.

To have a deeper understanding of the effect of the selective contact in combination with the Al_2O_3 mesoporous layer, we also measured PL properties of the meso-superstructured perovskite on top of SnO_2 and NiO_x. We note radiative recombination leading to PL occurs via band-to-band electron hole recombination, and non-radiative recombination, which leads to quenching of the PL, occurs via trap assisted recombination. We found that the perovskite PL is not strongly dependent on the Al_2O_3 thickness for the films processed on SnO_2 devices (**Figure S9a**), indicating that the trap assisted recombination is not strongly altered by the presence of the Al_2O_3. In contrast, there is a large increase of the PL for perovskite films processed on the 200 nm Al_2O_3 with the NiO_x configuration (**Figure S9b**). This is consistent with the electrons predominantly residing in the capping layer, where they can-not undergo trapping within the region of p-type perovskite within

the mesoporous scaffold. As shown in **Figure 4b** and **4c**, this had a marked difference in the charge carrier lifetime for both meso-superstructured configurations. The perovskite deposited on top of SnO_2 had much slower decay than the one deposited on NiO_x with a long tail independent of the Al_2O_3 thickness. Increasing the Al_2O_3 thickness on the NiO_x, increased the carrier lifetime, which is consistent with our absolute PL measurements. It is important to note that the long tail in the SnO_2 might indicate that there are shallow electron traps instead of deep electron traps, with a long de-trapping time.[31]

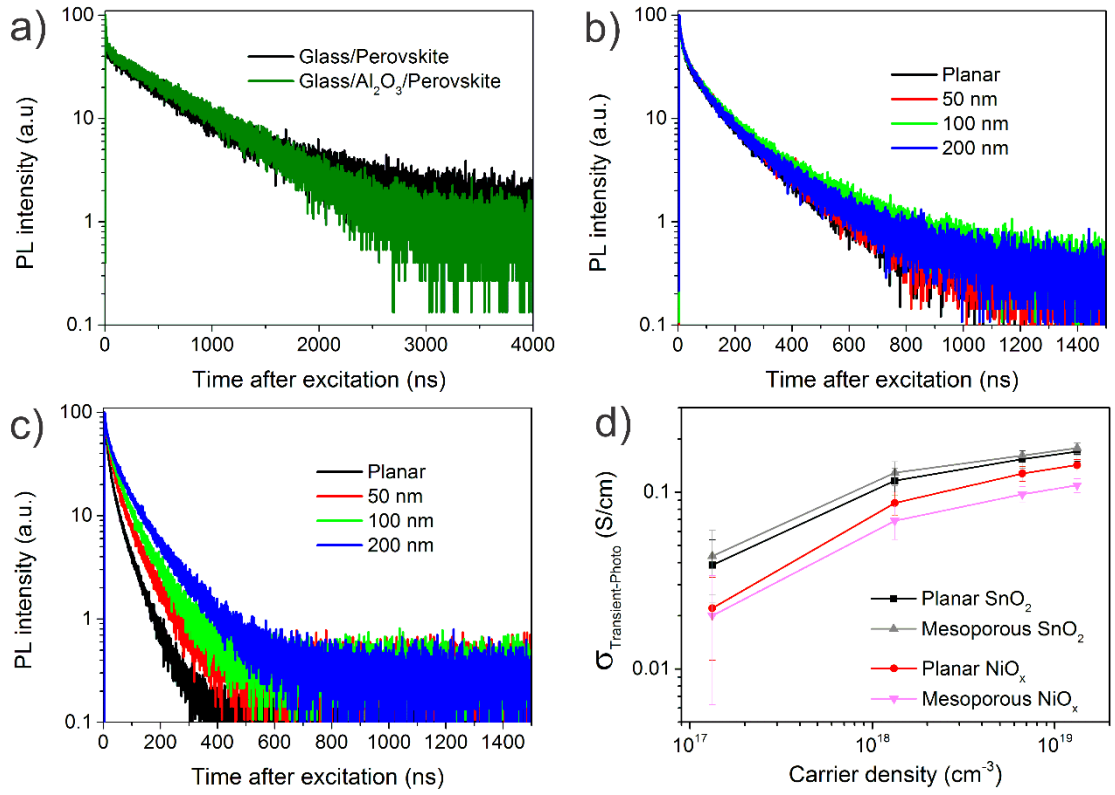

Figure 4. Time resolved PL for a) planar and mesoporous perovskite deposited on glass, and b) on SnO_2 and c) on NiO_x,respectively. d) Transient photocurrent devices perovskite in the planar and mesoporous n-i-p and p-i-n configuration.

A large density of sub-gap states, and the degree to which they are filled, should have an influence on long-range charge carrier transport. In order to probe this, we performed transient photoconductivity measurements as shown in **Figure 4d**. Excitation densities from 10^{17} cm^{-3} (similar to device operation) to 10^{19} cm^{-3} were used to monitor the photoconductivity. Higher photoconductivity was observed for the perovskite deposited on top SnO_2 compared to the NiO_x, and the difference in photoconductivity between the planar or meso-superstructured substrates is much larger for the films processed on NiO_x, than on SnO_2. These observations are consistent with more trapping, and shorter carrier lifetimes for the films processed on NiO_x, than on SnO_2. With the presence of the mesoporous Al_2O_3 having negligible impact on SnO_2, but increasing the trapping rate and reducing the carrier lifetime on NiO_x.

To summarize our findings, **Figure 5** shows the schematic representation of the proposed recombination mechanisms in which an intrinsic perovskite has sub-gap, trap mediated recombination with electron trapping being the primary decay pathway. For the case of the n-type perovskite infiltrated into the mesoporous layer, the non-radiative recombination is slower due to filled electron traps. While the p-type perovskite has more holes in the valence band and fewer filled electron traps, resulting in more rapid non-radiative recombination. Consequently, a reduced EQE at shorter wavelengths (corresponding to the light absorbed near the p-type contact-perovskite interface) was observed for the p-i-n devices. This results give new insights into the working mechanisms of different PSC architectures, paving the way for boosting the efficiency of this photovoltaic technology.

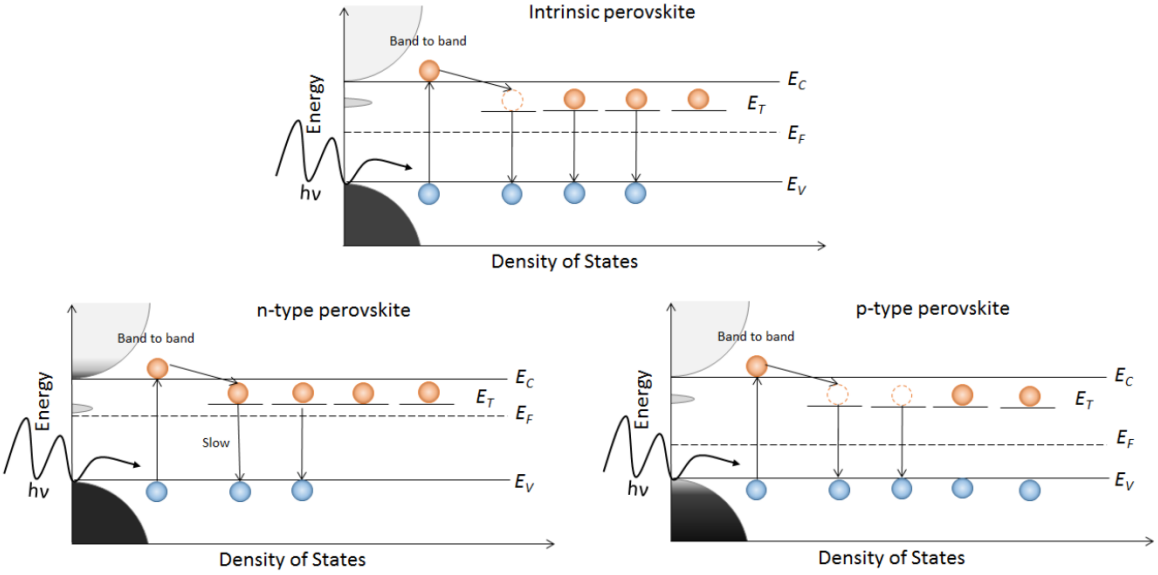

Figure 5. Schematic representation of the recombination process of a) an intrinsic perovskite, b) n-type and c) p-type perovskite.

4. Conclusions

While mesoporous perovskite solar cells have often outperformed their planar counterparts, the typical reasons given for this difference are reduced hysteresis and improved charge extraction, often heralding the mesoporous conductive TiO_2 responsible. Here, we discovered that mesoporous insulating Al_2O_3 layers provide a controllable method to strengthen the p- and n-nature of the perovskite absorber layer, contacting the selective charge extraction layer. Due to shallow electron traps being the primary recombination pathway in perovskite solar cells, devices benefit from n-type nature of the perovskite and show improved V_{oc} from better band alignment, increased J_{sc} from thicker films and improved charge collection, and therefore the highest power conversion efficiency of 21.0% for a meso-superstructured perovskite solar cell. Notably our findings indicate that the design criteria for an “ideal” perovskite solar cell should have an

extremely thin p-type region, so as to minimise current loss due to short electron diffusion in this region, but can have a much thicker n-type region. It is likely that this factor alone is why the n-i-p architectures still outperform the p-i-n architectures.

Supplementary information

Additional details of the KPFM characterization, cross-section SEM images of devices, photovoltaic parameters of p-i-n devices, reflectance, comparative JV curves including both, forward and reverse scans of the devices, and steady-state PL spectra of perovskite films.

Acknowledgements

We thank the Colombian “Departamento Nacional de Planeación”, SGR collaborative project 2013000100184 between Empresas Públicas de Medellin, Andercol S.A., Sumicol S.A.S., Universidad de Antioquia. K. S. is supported by Marshall Aid Commemoration Commission. This work was part funded by EPSRC UK. Comments from Dr. Rafael Betancur and Dr. Mario Mejia are greatly appreciated.

References

(1) Kojima, A.; Teshima, K.; Shirai, Y.; Miyasaka, T. Organometal Halide Perovskites as Visible-Light Sensitizers for Photovoltaic Cells. *J. Am. Chem. Soc.* **2009**, *131* (17), 6050–6051.

(2) Yang, W. S.; Park, B.-W.; Jung, E. H.; Jeon, N. J.; Kim, Y. C.; Lee, D. U.; Shin, S. S.; Seo, J.; Kim, E. K.; Noh, J. H.; et al. Iodide Management in Formamidinium-Lead-Halide-Based Perovskite Layers for Efficient Solar Cells. *Science* **2017**, *356* (6345), 1376–1379.

(3) NREL. Best Research-Cell Efficiencies http://www.nrel.gov/ncpv/images/efficiency_chart.jpg (accessed Aug 20, 2018).

(4) Park, N.-G. Perovskite Solar Cells: An Emerging Photovoltaic Technology. *Mater. Today* **2015**, *18* (2), 65–72.

(5) Mali, S. S.; Hong, C. K. P-i-n/n-i-p Type Planar Hybrid Structure of Highly Efficient Perovskite Solar Cells towards Improved Air Stability: Synthetic Strategies and Role of p-Type Hole Transport Layer (HTL) and n-Type Electron Transport Layer (ETL) Metal Oxides. *Nanoscale* **2016**, *8*, 10528–10540.

(6) Liang, P.-W.; Chueh, C.-C.; Williams, S. T.; Jen, A. K.-Y. Roles of Fullerene-Based

Interlayers in Enhancing the Performance of Organometal Perovskite Thin-Film Solar Cells. *Adv. Energy Mater.* **2015**, *5* (10), 1402321.
(7) Chen, W.; Wu, Y.; Liu, J.; Qin, C.; Yang, X.; Islam, A.; Cheng, Y.-B.; Han, L. Hybrid Interfacial Layer Leads to Solid Performance Improvement of Inverted Perovskite Solar Cells. *Energy Environ. Sci.* **2015**, *8* (2), 629–640.
(8) Snaith, H. J. Perovskites: The Emergence of a New Era for Low-Cost, High-Efficiency Solar Cells. *J. Phys. Chem. Lett.* **2013**, *4* (21), 3623–3630.
(9) Correa-Baena, J.-P.; Abate, A.; Saliba, M.; Tress, W.; Jesper Jacobsson, T.; Grätzel, M.; Hagfeldt, A. The Rapid Evolution of Highly Efficient Perovskite Solar Cells. *Energy Environ. Sci.* **2017**, *10* (3), 710–727.
(10) Kim, H.-S.; Lee, C.-R.; Im, J.-H.; Lee, K.-B.; Moehl, T.; Marchioro, A.; Moon, S.-J.; Humphry-Baker, R.; Yum, J.-H.; Moser, J. E.; et al. Lead Iodide Perovskite Sensitized All-Solid-State Submicron Thin Film Mesoscopic Solar Cell with Efficiency Exceeding 9%. *Sci. Rep.* **2012**, *2* (591), 1–9.
(11) Lee, M. M. M.; Teuscher, J.; Miyasaka, T.; Murakami, T. N. T. N.; Snaith, H. J. H. J. Efficient Hybrid Solar Cells Based on Meso-Superstructured Organometal Halide Perovskites. *Science (80-.).* **2012**, *338* (6107), 643–647.
(12) Liu, M.; Johnston, M. B.; Snaith, H. J. Efficient Planar Heterojunction Perovskite Solar Cells by Vapour Deposition. *Nature* **20139**, *501* (7467), 395–398.
(13) Ciro, J.; Mesa, S.; Uribe, J. I.; Mejía-Escobar, M. A.; Ramirez, D.; Montoya, J. F.; Betancur, R.; Yoo, H.-S.; Park, N.-G.; Jaramillo, F. Optimization of the Ag/PCBM Interface by a Rhodamine Interlayer to Enhance the Efficiency and Stability of Perovskite Solar Cells. *Nanoscale* **2017**, *9* (27), 9440–9446.
(14) Correa Baena, J. P.; Steier, L.; Tress, W.; Saliba, M.; Neutzner, S.; Matsui, T.; Giordano, F.; Jacobsson, T. J.; Srimath Kandada, A. R.; Zakeeruddin, S. M.; et al. Highly Efficient Planar Perovskite Solar Cells through Band Alignment Engineering. *Energy Environ. Sci.* **2015**, *8* (10), 2928–2934.
(15) Tan, H.; Jain, A.; Voznyy, O.; Lan, X.; García de Arquer, F. P.; Fan, J. Z.; Quintero-Bermudez, R.; Yuan, M.; Zhang, B.; Zhao, Y.; et al. Efficient and Stable Solution-Processed Planar Perovskite Solar Cells via Contact Passivation. *Science* **2017**, *355* (6326), 722–726.
(16) Ball, J. M.; Lee, M. M.; Hey, A.; Snaith, H. J. Low-Temperature Processed Meso-Superstructured to Thin-Film Perovskite Solar Cells. *Energy Environ. Sci.* **2013**, *6* (6), 1739.
(17) Ahn, N.; Son, D.-Y.; Jang, I.-H.; Kang, S. M.; Choi, M.; Park, N.-G. Highly Reproducible Perovskite Solar Cells with Average Efficiency of 18.3% and Best Efficiency of 19.7% Fabricated via Lewis Base Adduct of Lead(II) Iodide. *J. Am. Chem. Soc.* **2015**, *137* (27), 8696–8699.
(18) Turren-Cruz, S.-H.; Saliba, M.; Mayer, M. T.; Juárez-Santiesteban, H.; Mathew, X.; Nienhaus, L.; Tress, W.; Erodici, M. P.; Sher, M.-J.; Bawendi, M. G.; et al. Enhanced Charge Carrier Mobility and Lifetime Suppress Hysteresis and Improve Efficiency in Planar Perovskite Solar Cells. *Energy Environ. Sci.* **2018**, *11* (1), 78–86.
(19) Ke, W.; Fang, G.; Liu, Q.; Xiong, L.; Qin, P.; Tao, H.; Wang, J.; Lei, H.; Li, B.; Wan, J.; et al. Lowerature Solution-Processed Tin Oxide as an Alternative Electron Transporting Layer for Efficient Perovskite Solar Cells. *J. Am. Chem. Soc.* **2015**, *137* (21), 6730–6733.
(20) Anaraki, E. H.; Kermanpur, A.; Steier, L.; Domanski, K.; Matsui, T.; Tress, W.; Saliba,

M.; Abate, A.; Grätzel, M.; Hagfeldt, A.; et al. Highly Efficient and Stable Planar Perovskite Solar Cells by Solution-Processed Tin Oxide. *Energy Environ. Sci.* **2016**, *9* (10), 3128–3134.
(21) Ramirez, D.; Alejandro Mejía Escobar, M.; Montoya, J. F. J. F.; Jaramillo, F. Understanding the Role of the Mesoporous Layer in the Thermal Crystallization of a Meso-Superstructured Perovskite Solar Cell. *J. Phys. Chem. C* **2016**, *120* (16), 8559–8567.
(22) Ciro, J.; Ramírez, D.; Mejía Escobar, M. A.; Montoya, J. F.; Mesa, S.; Betancur, R.; Jaramillo, F. Self-Functionalization Behind a Solution-Processed NiOx Film Used As Hole Transporting Layer for Efficient Perovskite Solar Cells. *ACS Appl. Mater. Interfaces* **2017**, *9* (14), 12348–12354.
(23) Zhang, H.; Cheng, J.; Lin, F.; He, H.; Mao, J.; Wong, K. S.; Jen, A. K. Y.; Choy, W. C. H. Pinhole-Free and Surface-Nanostructured Niox Film by Room-Temperature Solution Process for High-Performance Flexible Perovskite Solar Cells with Good Stability and Reproducibility. *ACS Nano* **2016**, *10* (1), 1503–1511.
(24) Leijtens, T.; Stranks, S. D.; Eperon, G. E.; Lindblad, R.; Johansson, E. M. J.; McPherson, I. J.; Rensmo, H.; Ball, J. M.; Lee, M. M.; Snaith, H. J. Electronic Properties of Meso-Superstructured and Planar Organometal Halide Perovskite Films: Charge Trapping, Photodoping, and Carrier Mobility. *ACS Nano* **2014**, *8* (7), 7147–7155.
(25) Kronik, L.; Shapira, Y. Surface Photovoltage Spectroscopy of Semiconductor Structures: At the Crossroads of Physics, Chemistry and Electrical Engineering. *Surf. Interface Anal.* **2001**, *31* (10), 954–965.
(26) Ciro, J.; Mesa, S.; Montoya, J. F.; Uribe, J. I.; Betancur, R.; Jaramillo, F. Simultaneous Top and Bottom Perovskite Interface Engineering by Fullerene Surface Modification of Titanium Dioxide as Electron Transport Layer. *ACS Appl. Mater. Interfaces* **2017**, *9* (35), 29654–29659.
(27) Liqiang, J.; Xiaojun, S.; Jing, S.; Weimin, C.; Zili, X.; Yaoguo, D.; Honggang, F. Review of Surface Photovoltage Spectra of Nano-Sized Semiconductor and Its Applications in Heterogeneous Photocatalysis. *Sol. Energy Mater. Sol. Cells* **2003**, *79* (2), 133–151.
(28) Leijtens, T.; Eperon, G. E.; Barker, A. J.; Grancini, G.; Zhang, W.; Ball, J. M.; Kandada, A. R. S.; Snaith, H. J.; Petrozza, A. Carrier Trapping and Recombination: The Role of Defect Physics in Enhancing the Open Circuit Voltage of Metal Halide Perovskite Solar Cells. *Energy Environ. Sci.* **2016**, *9* (11), 3472–3481.
(29) Stranks, S. D.; Burlakov, V. M.; Leijtens, T.; Ball, J. M.; Goriely, A.; Snaith, H. J. Recombination Kinetics in Organic-Inorganic Perovskites: Excitons, Free Charge, and Subgap States. *Phys. Rev. Appl.* **2014**, *2* (3), 034007.
(30) Zhang, W.; Pathak, S.; Sakai, N.; Stergiopoulos, T.; Nayak, P. K.; Noel, N. K.; Haghighirad, A. A.; Burlakov, V. M.; deQuilettes, D. W.; Sadhanala, A.; et al. Enhanced Optoelectronic Quality of Perovskite Thin Films with Hypophosphorous Acid for Planar Heterojunction Solar Cells. *Nat. Commun.* **2015**, *6*, 10030.
(31) Brenes, R.; Guo, D.; Osherov, A.; Bulovi, V.; Savenije, T. J.; Stranks, S. D. Metal Halide Perovskite Polycrystalline Films Exhibiting Properties of Single Crystals. *Joule* **2017**, *1* (1), 155–167.

Table of Contents